Picomolar sensitivity MRI and photoacoustic imaging of cobalt nanoparticles

Louis-S. Bouchard[a,1], M. Sabieh Anwar[b,1], Gang L. Liu[c,2], Byron Hann[c], Z. Harry Xie[d], Joe W. Gray[c], Xueding Wang[e,1], Alexander Pines[f,g,1], and Fanqing Frank Chen[c,h,i,1]

[a]Department of Chemistry and Biochemistry, University of California, Los Angeles, CA 90095; [b]School of Science and Engineering, Lahore University of Management Sciences, Opposite Sector U, D.H.A. Lahore 54792, Pakistan; [c]Comprehensive Cancer Center, University of California, San Francisco, CA 94143; [d]Minispec Division, Bruker Optics, Inc., 2700 North Crescent Ridge Drive, The Woodlands, TX 77381; [e]Department of Radiology, University of Michigan, Ann Arbor, MI 48109-0553; [f]College of Chemistry, University of California, Berkeley, CA 94720; [g]Materials Sciences Division and [h]Life Sciences Division, Lawrence Berkeley National Laboratory, Berkeley, CA 94720; and [i]Zhejiang California Nanosystems Institute, Zhejiang University, Hangzhou 310029, People's Republic of China

Multimodality imaging based on complementary detection principles has broad clinical applications and promises to improve the accuracy of medical diagnosis. This means that a tracer particle advantageously incorporates multiple functionalities into a single delivery vehicle. In the present work, we explore a unique combination of MRI and photoacoustic tomography (PAT) to detect picomolar concentrations of nanoparticles. The nanoconstruct consists of ferromagnetic (Co) particles coated with gold (Au) for biocompatibility and a unique shape that enables optical absorption over a broad range of frequencies. The end result is a dual-modality probe useful for the detection of trace amounts of nanoparticles in biological tissues, in which MRI provides volume detection, whereas PAT performs edge detection.

dual-modality imaging | ferromagnetic nanoparticle | molecular imaging | MRI contrast | photoacoustic tomography

We have synthesized nanoparticles for dual-modality (1–7) MRI and photoacoustic tomography (PAT). The incorporation of MRI and PAT into a single probe offers the unique possibility of combining the complementary strategies of contrast-based volume imaging and edge detection. Our nanoconstruct consists of zero-valence ferromagnetic cobalt (Co) particles (8) with a gold (Au) coating for biocompatibility and a unique shape rendering increased optical absorption over a broad range of frequencies (9–19). This research theme follows the rapid developments in nanotechnology, diagnostic radiology, and targeted molecular imaging (20), whereby nanoparticulate contrast agents, with the desirable properties of high chemical specificity, biocompatibility, and a reasonable half-life, are administered within a specific region of interest. In nanoparticle-based imaging studies, higher particle concentrations lead to better signal-to-noise contrasts, but this also poses a tradeoff with the toxicity. Therefore, one of the most important parameters when developing particle-based contrast is the safest and lowest nanoparticle concentration that offers sufficient contrast sensitivity.

In MRI, magnetic materials such as gadolinium chelates and magnetic nanoparticles are often used (21–23) to enhance image contrast. The magnetic nanoparticles are passivated by biocompatible coatings such as dextrin, citrate, polystyrene/divinylbenzene, and elemental gold. These coatings also detoxify the particles, resulting in enhanced lifetimes in vivo. Typical examples of magnetic nanoparticulate core-shell configurations include magnetite–dextrin, magnetite–silica (24) and iron–gold (25).

Laser-based PAT (9–19) is a hybrid imaging modality [see supporting information (SI) Fig. S1]. It uses a pulsed laser source to illuminate a biological sample. Light absorption by the tissue results in a transient temperature rise on the order of 10 mK. The rapid thermoelastic expansion excites ultrasonic waves that are measured by using broadband ultrasonic transducers conformally arranged around the sample. Finally, a modified back-projection reconstruction algorithm (26) is used to construct a map of the distribution of the optical energy deposition within the sample. The

spatial resolution of PAT is not limited by optical diffusion, but instead by the bandwidth of the acoustic detectors. It has been shown that PAT can depict subsurface tissue structures and functional changes noninvasively with resolution up to 100 μm (14, 15). Like other optical modalities, PAT is highly sensitive in mapping and quantifying the dynamic distribution of optical contrast agents such as metallic nanocolloids and organic dyes (16–19, 27).

In the present work, we have fabricated a composite-material nanoparticle, which we call "nanowonton." The nanowonton has a Co core and an Au thin-film coating and is a construct similar to the Chinese eatable called the wonton (see Fig. 1 and Fig. S2). The nanowontons have been characterized by scanning and transmission electron microscopies, absorption spectroscopy, and NMR relaxometry (Fig. 2). The nanowonton is shown to exhibit a combination of ferromagnetic and optical responses (Fig. 2), making it amenable to dual-modality MRI and PAT studies. NMR T_2 relaxivity measurements reveal a per-particle relaxivity of 1×10^7 $s^{-1}mM^{-1}$ (Table 1).

Previously, the oxidation-induced instability and toxicity of Co nanoparticles have prohibited their wide use as MRI contrast agents, but in the present case, the Au coating circumvents this issue. Furthermore, the shape and thickness of the Au capping layer are designed so that the center of its optical absorption range matches the near infrared laser excitation wavelength used in PAT imaging (700 nm) optimizing the photothermal response. We have also reported the geometry-dependent optical absorption for similarly shaped nanostructures such as nanocrescents (28). The nanowonton design provides wavelength tunability for PAT (Fig. S3) and can be further improved through control of the fabrication procedure.

The PAT imaging contrast is demonstrated in Fig. 3A, for an porcine gel containing several inclusions of different nanowonton concentrations. The inclusion with a nanowonton concentration of 13 pM can hardly be recognized from the background, leading us to conclude that this PAT system has a detection sensitivity of the order of 25 pM. Spin echo MRI images of Co nanowonton agarose gel phantoms A and B are shown in Fig. 4A and B. Spin echo images show that higher concentrations lead to shorter T_2 values for the
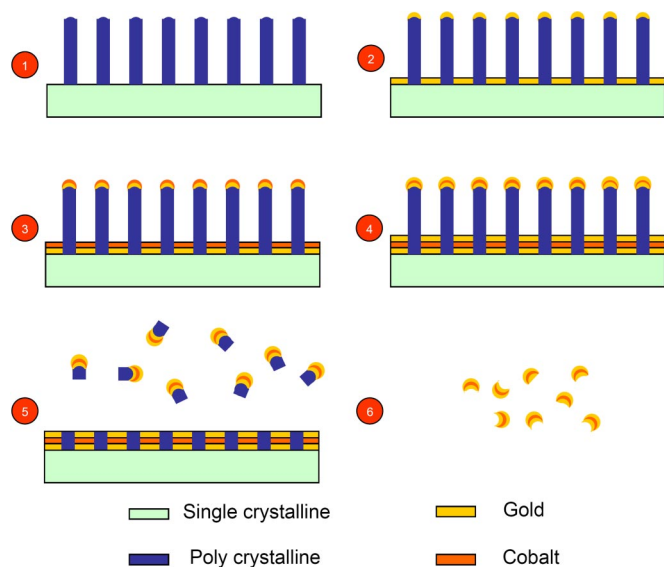
Fig. 1. Fabrication procedure of the nanowontons including 6 steps: (1) Etching polysilicon nanopillars on the surface of single crystalline silicon wafer (for simpler presentation, we omitted from the illustration the preparatory step of depositing 5 nm of chromium before going to step 2, see *Methods*); (2) deposition of a 10-nm gold thin film; (3) deposition of 10-nm cobalt thin film; (4) deposition of 10-nm gold thin film; (5) etching polysilicon nanopillars in KOH batch solution; and (6) complete removal of polysilicon and chromium by KOH etching and separation of nanowontons.

water protons. The smallest detectable concentration is 2.5 pM and the contrast with respect to 5 pM is also clearly visible in Fig. 4 *B* and *D*.

A T_2-weighted spin echo image from a slice through the mouse's leg muscles is shown in Fig. 5. The injection of PBS-buffered Co nanoparticles at 50 pM concentration results in a substantial drop in the MR signal in this region whereas the control injection with PBS shows no such contrast enhancement. In Fig. S4, PAT images acquired before and after a rat tail injection show the type of contrast enhancement which can be expected from a local injection of 100 pM contrast agent. Because of high-frequency ultrasound detection, the PAT modality is generally better suited at delineating edges at the location of the contrast. These nanowonton particles advantageously combine the strengths of both MRI and PAT modalities into a single delivery vehicle.

This dual-modality PAT/MRI contrast agent demonstrates, so far, the most sensitive detection experiment of magnetic nanoparticles with particle concentrations in the picomolar and tens of picomolars range. The particles may even be used for stand-alone MRI or PAT. For example, in the MRI studies, the T_2 contrast is clearly visible to concentrations as low as 2.5 pM in phantoms and 50 pM in tissues. These detection thresholds are 7 orders of magnitude better than those demonstrated by Lu *et al.* (23) for monocrystalline iron oxide particles. Our T_2 relaxivity (see Table 1) per-particle concentration is 5 orders of magnitude better than the cited work. The particle relaxivity and T_2-weighted MRI detection threshold are also better than those demonstrated by Cho *et al.* (25) for 18 nm-diameter Fe/Au nanoparticles. This degree of sensitivity is, to our knowledge, unprecedented and compares with sensitivities approaching those of radioactive labels. This improved performance is in large part contributed by our choice of a ferromagnetic material, cobalt, which has a saturation magnetization 3.42 times larger than magnetite, leading to a per-particle relaxivity that is nearly 12 times larger. Because T_2-weighted MRI depends exponentially on the relaxation rate, this leads to a substantial difference in contrast observed in our experiments. We refer the reader to the SI section for a more extensive discussion of relaxivity effects, including a comparison with results from other agents reported in the literature.

The highly stable, thin (10 nm) film (Au) coating provides biocompatibility, as demonstrated by experimental results (Fig. S5). Furthermore, the Au thin film deposition process can be well controlled to allow tunable absorption spectra, allowing PAT at
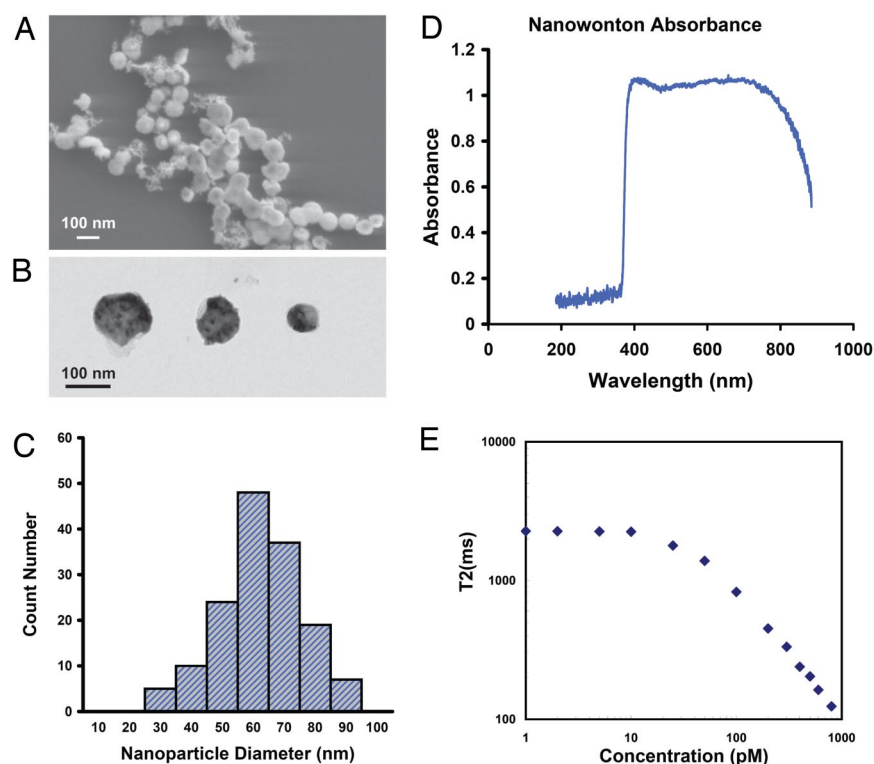

Fig. 2. Characterization of the cobalt nanowontons. (*A*) Scanning electron microscopy image of nanowontons. (*B*) Transmission electron microscopy image of 3 nanowontons in various diameters; notice that the lighter regions in the nanoparticle are relatively hollow, and are responsible for photothermal tuning properties of the nanowonton (38). (*C*) Particle diameter distribution of 150 nanowontons. Because of the inhomogeneous polysilicon nanopillar diameter, the size of the nanowontons varies from 30 to 90 nm, and the average diameter is 60 nm. (*D*) Absorption spectrum of nanowonton, medium peak wavelength is ≈700 nm. (*E*) Spin–spin relaxation time T_2 measured at 20 MHz proton frequency and 37 °C. T_2 begins to change when the concentration exceeds 20 pM. Note that although 20 MHz is much less than 300 MHz (used for the MRI), this gives a lower bound on relaxivity and shows that the contrast works even at low fields, such as those from portable NMR devices.

Table 1. T_2 relaxivity per particle concentration is calculated to be 1×10^7 s^{-1}mM^{-1}

Sample no.	Conc, pM	T_2, ms	Conc, mM	$1/T_2$, s^{-1}
1	1,000	123	0.000001	8.1301
2	800	124	0.0000008	8.0645
3	600	163	0.0000006	6.1350
4	500	204	0.0000005	4.9020
5	400	239	0.0000004	4.1841
6	300	333	0.0000003	3.0030
7	200	451	0.0000002	2.2173
8	100	828	0.0000001	1.2077
9	50	1384	0.00000005	0.7225
10	25	1788	0.000000025	0.5593
11	10	2250	0.00000001	0.4444
12	5	2258	0.000000005	0.4429
13	2	2268	0.000000002	0.4409
14	1	2270	0.000000001	0.4405

The T_2 reaches saturation point above 800 pM, so the 1,000-pM data point was excluded from the fit to obtain linearity for calculating $1/T_2$.

different optical wavelengths (see Fig. S3). It has been demonstrated that a variety of gold nanocolloids are already entering in vivo clinical trials (19, 29–33). Among them, Au nanorods present particularly good optical absorption in the near-infrared region, tunable by changing the aspect ratio. It has already been demonstrated that gold nanorod contrast agents can be imaged with PAT, both ex and in vivo (34, 35). Our study has shown that the sensitivity of PAT in imaging the nanowonton is equivalent to that for gold nanorods. In fact, the MRI contrast is also expected to be strongly dependent on the shape of the nanoconstruct. It is envisaged that nanorods or needle-shaped structures can elicit greater contrast because of larger shape-induced susceptibility gradients. The present nanowonton shape is, to first order, a compromise between optical and magnetic responses. However, further work on shape optimization will be required to conclusively comment on this. Furthermore, the Au sandwich structure also allows additional tuning of absorbed wavelengths (28, 36, 37). This can further improve the sensitivity of the PAT technique. Last, the Au coatings are especially attractive because of the possibility of conjugating the particles with specific molecules such as antibodies, specific ligands, thiol functional groups and therapeutic drugs, opening up prospects for targeted molecular imaging (20). An additional imaging modality built into our nanoconstruct is the optical thermal conversion capability making these structures highly suited for photothermal therapy (32, 38–41).

Methods

For additional information on materials and methods used, see *SI Text*.

Fabrication of the Nanowontons. The schematic diagram of the fabrication procedure is illustrated in Fig. 1. First, a batch-fabricated vertical silicon nanopillar array was fabricated on the surface of a 4-inch diameter silicon wafer. The coverage of the nanopillar structure was >90% of the total wafer surface area. On the top of each silicon nanopillar, there was a spherical silicon oxide nanostructure. Four metallic layers of 5-nm chromium, 10-nm gold, 10-nm cobalt, and 10-nm gold were sequentially deposited on the wafer surface. However, after deposition, the sidewalls of all of the nanopillars remained exposed. The silicon wafer was therefore immersed in a 10% KOH bath solution at 80 °C, etching away the nanopillars from the unprotected sidewalls in 10 min, The multilayer metallic nanostructure on the top of the nanopillars was lifted off and suspended in the KOH bath solution. Because silicon oxide and chromium were also etched away by KOH, only the gold–cobalt–gold sandwich nanostructures, the nanowontons, remained in solution. These were finally separated by centrifugation. The SEM, TEM, and size distribution measurements are shown in Fig. 2 *A–C*. After fabrication, these samples were chemically analyzed by inductively coupled plasma mass spectrometry (ICP-MS), measuring the total amount of Co or Au ions. By assuming bulk parameters of the materials and the size of the nanoparticles, we deduced the mass of Co and Au per nanoparticle, and calculated the nanoparticle concentration.

PAT System. The PAT system is schematically shown in Fig. S1. An OPO (Vibrant B; Opotek) pumped by an Nd/YAG laser (Brilliant B; Bigsky) was used to provide laser pulses with a repetition rate of 10 Hz and a pulse width of 5 ns. In this study, the wavelength of the laser light was tuned to 700 nm, which was in the near-infrared region and enabled good penetration in biological tissues. The laser beam, after being expanded and homogenized, illuminated the imaged sample with an input energy density of ≈10 mJ/cm², well below the American National Standards Institute safety limit of 22 mJ/cm² at the applied wavelength. The laser light penetrated into the sample and generated photoacoustic signals that were scanned by an ultrasonic transducer (XMS-310; Panametrics) with a center frequency at 10 MHz and a receiving bandwidth of 100%. To realize 2D cross-sectional imaging, the sample was rotated axially in the *xy* plane while the transducer and the laser beam were kept static. To couple the signals, the sample and the transducer were immersed in water. After a preamplifier (PR5072; Panametrics), the detected signals were digitized by an oscilloscope (TDS 540B; Tektronics) and then collected by a computer. The current PAT system exhibits spatial resolution of 200 μm in the *xy* plane, which has been verified by measuring the line spread function (LSF) (40).

Photoacoustic Imaging on Phantoms. To demonstrate the PAT imaging contrast, we constructed a phantom made of 5% porcine gel in which 4 inclusions with different concentrations of nanowontons are embedded (Fig. 3). Cylindrical-shaped phantoms with a 20-mm diameter were made from porcine gel. Spherical-shaped droplets with a size of 2.8 mm were made with the same gel and contained different concentrations of the contrast agent. These droplets were embedded 1 cm deep in the phantoms. For example, the phantom shown in Fig. 3 contains 4 such embedded droplets, where the nanowonton concentrations were 100, 50, 25, and 13 pM. The corresponding PAT image is shown in Fig. 3*A*,
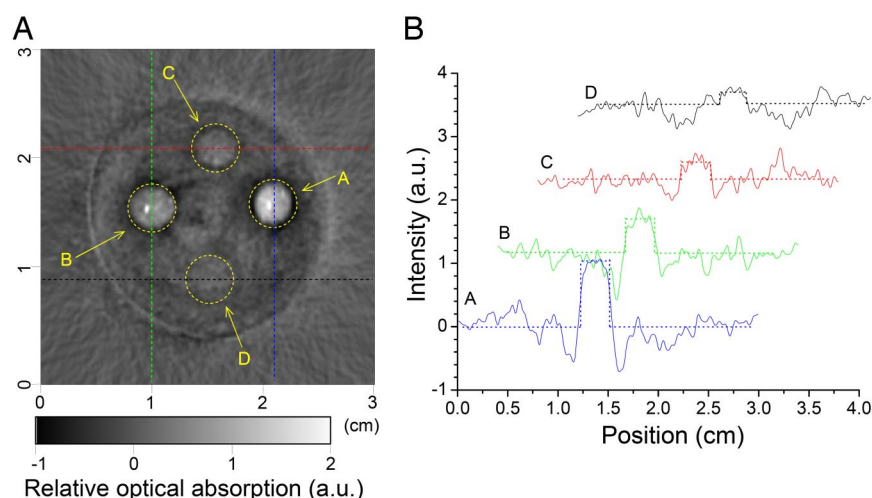
Fig. 3. Photoacoustic imaging of nanowonton phantom gels. (*A*) PAT image of 4 absorbing objects containing nanowonton contrast agent embedded in a gel phantom (5% agarose). The concentrations of nanowontons were 100, 50, 25, and 13 pM, respectively, for objects A, B, C, and D. (*B*) Intensity profiles extracted from the image along 4 lines (horizontal and vertical dashed lines indicated on the image) going through the absorbing centers are plotted to highlight the visibility of nanowonton inclusions in the reconstructed image. With a CNR close to 1, the object D, where the nanowonton concentration is 13 pM, can hardly be recognized from the background, showing that the current PAT system has detection sensitivity on the order of 25 pM.
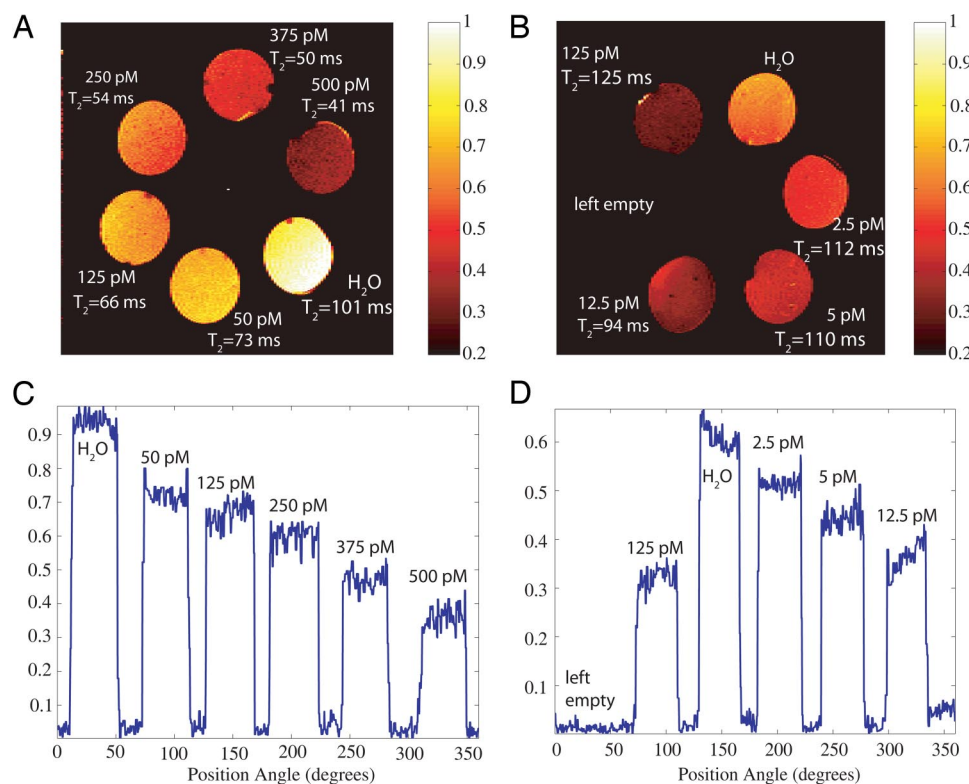
Fig. 4. MRI of nanowonton gel phantoms. The nanowonton gels are arranged along the perimeter of a circle. (*A* and *B*) Spin-echo images for the phantoms A and B, respectively, with an echo time (TE) of 50 ms and recycle time (TR) of 1 s. The higher-concentration samples appear darker in the images, with doped water used as a control and exhibiting the strongest T_2-weighted intensity. The concentrations of the gels are given in the figure along with the T_2 values that are deduced from a 7-point curve-fitting procedure. The field of view for this image is 3 × 3 cm, the number of points is 256 × 128, and the slice thickness is 1 mm. (*C* and *D*) Intensity profiles for the images in *A* and *B*. The relative intensities along a circular contour drawn through the middle of the gels are plotted as a function of the gel azimuthal angle from the *x* axis. The nanoparticles contrast remains detectable down to 2.5 pM. The images for phantom A and B are plotted to different (normalized) scales.
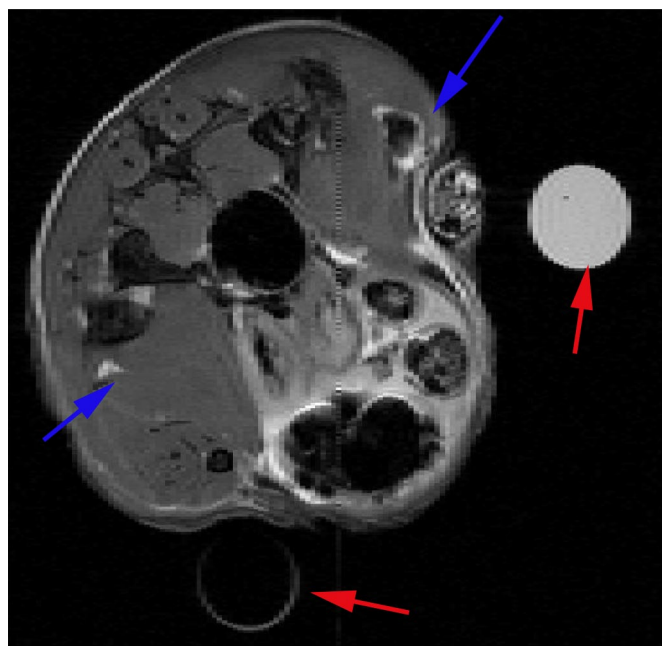

Fig. 5. Transverse (axial) MRI image in mouse leg muscle injected with Co nanoparticles in PBS solution. The position of the blue arrows indicates the sites of injection for the Co nanoparticles (upper right corner) and the PBS control (lower left corner). Two water-carrying test tubes are also visible in the scans for purposes of MRI slice alignment (red arrows). MRI parameters were: TE = 50 ms; TR = 1 s; field of view is 2.6 cm × 2.6 cm, and slice thickness is 0.5 mm.

the locations of the objects being marked with dashed circles. In Fig. 3*A*, we have also quantified the contrast-to-noise ratio (CNR) = $(S_o − S_b)/\sigma$, where S_o is the average intensity within the object, S_b is the average intensity within the background defined by the mean of all of the pixels in the image beyond the big dashed circle (i.e., the area out of the gel phantom), and σ is the standard deviation. The computed CNRs for the objects A, B, C, and D are 10.6, 5.7, 2.1, and 1.0. It is clear that the objects A, B, and C have been imaged with sufficient optical absorption contrast.

MRI of the Phantoms. For the phantom MRI studies, 6 holes were drilled into a (≈3 cm diameter) Teflon cylinder, azimuthally distributed around the center. The phantom is shown in Fig. 4. Each hole was 5 mm in diameter and ≈1 cm deep. Two similar pieces (A and B) were machined. Nanocolloidal solutions of the nanowonton in (5%) agarose gel were prepared in concentrations of 500, 375, 250, 125, 50, 12.5, 5, and 2.5 pM. The agarose gel was heated until it became transparent, and the nanoparticles were subsequently transferred to the hot agarose, preparing the desired concentrations. Precise volumes of the nanocolloids were then slowly transferred to the cylindrical recesses and allowed to cool in ambient conditions, ensuring that no air bubbles were formed during the cooling. The solutions were intermittently pried to ensure that the distribution of the nanowontons would be kept as uniform as possible. The tops and bottoms of the phantoms were sealed with polystyrene to prevent leakage during phantom handling. The phantom A contained the concentrations 500, 375, 250, 125, and 50 pM, whereas B contained 125, 12.5, 5, and 2.5 pM. The latter had 1 cylinder empty, and each of the phantoms was also loaded with 0.6 mM $MnCl_2$ doped water to act as the control reference.

The MRI was performed in a 300-MHz NMR spectrometer (Varian Inova) equipped with triple-axis magnetic field gradients. The phantoms were imaged by using a spin-echo pulse sequence, with slice selection along the *z* axis, phase encoding along the *y* axis, and readout along the *x* axis. We used an echo time (TE) of 50 ms and recycle time (TR) of 1 s. The field of view was 3 × 3 cm, the number of points was 256 × 128, and the slice thickness along the *z* direction was 1 mm. T_2 measurements were also performed by repeating the spin echo sequence with varying TEs; the values used were 10, 30, 40, 50, 100, 150, and 200 ms.

MRI on Mouse Muscle. For the animal studies, the mouse was i.p. anesthetized with 400 μL of Avertin. After 5 min, 50 μL of 60-nm-sized gold-coated Co nanoparticles at 50 pM in a solution of PBS were intramuscularly injected into the leg. As a control, PBS solution without the nanoparticles was also injected in the diametrically opposite position to the site of injection of the cobalt nanowonton. After an additional 10 min, the mouse was killed and placed into the vertical bore of the Varian 300-MHz NMR spectrometer. The mouse tail was then imaged by using a T_2-weighted spin-echo sequence. Multiple transverse slices were imaged, the slice thickness (along the z direction) being 0.5 mm, the TR was 1 s, the number of points was 256 × 128, and the field of view was 2.6 × 2.6 cm.

1. T Al-Jamal W, Kostarelos, K (2007) Liposome-nanoparticle hybrids for multimodal diagnostic and therapeutic applications. *Nanomedicine-UK* 2:85–98.
2. Jaffer FA, et al. (2006) Cellular imaging of inflammation in atherosclerosis using magnetofluorescent nanomaterials. *Mol Imaging* 5:85–92.
3. Mulder WJM, et al. (2005) MR molecular imaging and fluorescence microscopy for identification of activated tumor endothelium using a bimodal lipidic nanoparticle. *FASEB J* 19:doi:10.1096/fj.05–4145fje.
4. Tan WB, Zhang Y (2007) Multi-functional chitosan nanoparticles encapsulating quantum dots and Gd-DTPA as imaging probes for bio-applications. *J Nanosci Nanotechno* 7:2389–2393.
5. Dosev D, et al. (2007) Magnetic/luminescent core/shell particles synthesized by spray pyrolysis and their application in immunoassays with internal standard. *Nanotechnology* 18:055102.
6. Prinzen L, et al. (2007) Optical and magnetic resonance imaging of cell death and platelet activation using annexin A5-functionalized quantum dots. *Nano Lett* 7:93–100.
7. Medarova Z, Pham W, Kim Y, Dai GP, Moore A (2006) In vivo imaging of tumor response to therapy using a dual-modality imaging strategy. *Int J Cancer* 118:2796–2802.
8. Bala T, Arumugam SK, Pasricha R, Prasad BLV, Sastry M (2004) Foam-based synthesis of cobalt nanoparticles and their subsequent conversion to Co core Ag shell nanoparticles by a simple transmetallation reaction. *J Mater Chem* 14:1057–1061.
9. Hoelen CGA, de Mul FFM, Pongers R, Dekker A (1998) Three-dimensional photoacoustic imaging of blood vessels in tissue. *Opt Lett* 23:648–650.
10. Oraevsky AA, Jacques SL, Tittel FK (1997) Measurement of tissue optical properties by time-resolved detection of laser-induced transient stress. *Appl Optics* 36:402–415.
11. Kruger RA, Liu PY, Fang YR, Appledorn CR (1995) Photoacoustic Ultrasound (PAUS) - Reconstruction Tomography. *Medical Physics* 22:1605–1609.
12. Andreev VG, Karabutov AA, Oraevsky AA (2003) Detection of ultrawide-band ultrasound pulses in optoacoustic tomography. *IEEE T. Ultrason. Ferr.* 50:1383–1390.
13. Kolkman RGM, Hondebrink E, Steenbergen W, de Mul FFM. (2003) In vivo photoacoustic imaging of blood vessels using an extreme-narrow aperture sensor. *IEEE J. Sel. Top. Quant.* 9:343–346.
14. Wang XD, et al. (2004) Noninvasive photoacoustic angiography of animal brains in vivo with near-infrared light and an optical contrast agent. *Opt Lett* 29:730–732.
15. Wang XD, Pang YJ, Ku G, Stoica G, Wang LHV (2003) Three-dimensional laser-induced photoacoustic tomography of mouse brain with the skin and skull intact. *Opt Lett* 28:1739–1741.
16. Ku G, Wang XD, Stoica G, Wang LHV (2004) Multiple-bandwidth photoacoustic tomography. *Physics in Medicine and Biology* 49:1329–1338.
17. Ku G, Wang XD, Xie XY, Stoica G, Wang LHV (2005) Imaging of tumor angiogenesis in rat brains in vivo by photoacoustic tomography. *Appl Optics* 44:770–775.
18. Wang XD, et al. (2003) Noninvasive laser-induced photoacoustic tomography for structural and functional in vivo imaging of the brain. *Nat Biotechnol* 21:803–806.
19. Wang YW, et al. (2004) Photoacoustic tomography of a nanoshell contrast agent in the in vivo rat brain. *Nano Lett* 4:1689–1692.
20. Wickline SA, Lanza GM (2002) Molecular imaging, targeted therapeutics, and nanoscience. *J Cell Biochem*, 90–97.
21. Cunningham CH, et al. (2005) Positive contrast magnetic resonance imaging of cells labeled with magnetic nanoparticles. *Magnet Reson Med* 53:999–1005.
22. Kim DK, et al. (2001) Characterization and MRI study of surfactant-coated superparamagnetic nanoparticles administered into the rat brain. *J Magn Magn Mater* 225:256–261.
23. Lu J, et al. (2006) Solid-state synthesis of monocrystalline iron oxide nanoparticle based ferrofluid suitable for magnetic resonance imaging contrast application. *Nanotechnology* 17:5812–5820.
24. Lu CW, et al. (2007) Bifunctional magnetic silica nanoparticles for highly efficient human stem cell labeling. *Nano Lett* 7:149–154.
25. Cho SJ, Jarrett BR, Louie AY, Kauzlarich SM (2006) Gold-coated iron nanoparticles: a novel magnetic resonance agent for T_1 and T_2 weighted imaging. *Nanotechnology* 17:640–644.
26. Xu MH, Wang LHV (2005) Universal back-projection algorithm for photoacoustic computed tomography. *Phys Rev E* 71:016706.
27. Copland JA, et al. (2004) Bioconjugated gold nanoparticles as a molecular based contrast agent: Implications for imaging of deep tumors using optoacoustic tomography. *Mol Imaging Biol* 6:341–349.
28. Lu Y, Liu GL, Kim J, Mejia YX, Lee LP (2005) Nanophotonic crescent moon structures with sharp edge for ultrasensitive biomolecular detection by local electromagnetic field enhancement effect. *Nano Lett* 5:119–124.
29. Durr NJ, et al. (2007) Two-photon luminescence imaging of cancer cells using molecularly targeted gold nanorods. *Nano Lett* 7:941–945.
30. Huff TB, et al. (2007) Hyperthermic effects of gold nanorods on tumor cells. *Nanomedicine-UK* 2:125–132.
31. Lee KS, El-Sayed MA (2006) Gold and silver nanoparticles in sensing and imaging: Sensitivity of plasmon response to size, shape, and metal composition. *J Phys Chem B* 110:19220–19225.
32. Loo C, Lowery A, Halas N, West J, Drezek R (2005) Immunotargeted nanoshells for integrated cancer imaging and therapy. *Nano Lett* 5:709–711.
33. Kim K, et al. (2007) Photoacoustic imaging of early inflammatory response using gold nanorods. *Appl Phys Lett* 90:223901.
34. Chamberland DL, et al. (2008) Photoacoustic tomography of joint aided by Etanercept conjugated gold nanoparticle contrast agent - an ex vivo preliminary rat study. *Nanotechnology* 19:95–101.
35. Eghtedari M, et al. (2007) High sensitivity of in vivo detection of gold nanorods using a laser optoacoustic imaging system. *Nano Lett* 7:1914–1918.
36. Liu GL, et al. (2006) A nanoplasmonic molecular ruler for measuring nuclease activity and DNA footprinting. *Nat Nanotechnol* 1:47–52.
37. Liu GL, et al. (2007) Peptide-nanoparticle hybrid SERS probes for optical detection of protease activity. *J Nanosci Nanotechno* 7:2323–2330.
38. Liu GL, Kim J, Lu Y, Lee LP (2006) Optofluidic control using photothermal nanoparticles. *Nat Mater* 5:27–32.
39. Loo C, et al. (2004) Nanoshell-enabled photonics-based imaging and therapy of cancer. *Technol Cancer Res T* 3:33–40.
40. Chou CH, Chen CD, Wang CRC. (2005) Highly efficient, wavelength-tunable, gold nanoparticle based optothermal nanoconvertors. *J Phys Chem B* 109:11135–11138.
41. Hirsch LR, et al. (2003) Nanoshell-mediated near-infrared thermal therapy of tumors under magnetic resonance guidance. *P Natl Acad Sci USA* 100:13549–13554.

CHEMISTRY

Supporting Information

Bouchard et al. 10.1073/pnas.0813019106

SI Text

MRI Contrast Sensitivity. It is instructive to examine possible reasons for the superior MRI contrast enhancement. Larger (micron-size) superparamagnetic particles can be manufactured by embedding nanoparticles into a polymer matrix. It is unclear; however, that the net moment would be expected to increase linearly with the size of the construct as due to the misalignment of the multiple magnetic domains, some amount of cancellation will take place, leading to a smaller net magnetic moment per unit volume and also per particle. This is true even in the presence of a strong magnetic field as used in MRI, because the anisotropy energy of the material which causes the random reorientation of single domains is typically much larger than the Zeeman energy. When comparing our Co nanowonton to conventional small paramagnetic iron oxide (SPIO) particles under an applied field that saturates the magnetization (including any hysteresis effect), the relevant quantity for molecular imaging purposes, where a binding event involves one ligand moiety per target molecule, is the per-particle relaxivity. In a homogeneous solution of ferromagnetic particles, the per-particle relaxivity for water is proportional to the square of the magnetic moment of relaxing centers. The saturation magnetization of fcc-Co is 3.42 times higher than magnetite (Fe_3O_4) (1), which implies a per-particle relaxivity that is nearly 12 times larger than magnetite. This has important implications for T_2-weighted MRI, which depends exponentially on the relaxation rate. For example, a 1 μM concentration of Co nanowonton particles with T_2 relaxivity of 1×10^7 $s^{-1} \cdot mM^{-1}$ (as measured experimentally for our nanowonton) and an echo time of 50 ms produces an exponential decay factor that is 100 times larger than for magnetite. This is how substantial improvements in NMR signal changes can be obtained for the same particle size. Regarding our actual numbers, the measured T_2 relaxivity is 1×10^7 $s^{-1} \cdot mM^{-1}$, which is a 5-orders-of-magnitude higher "per-particle" relaxivity than the monocrystalline iron oxide nanoparticles (MION) of ref. 2, in which a rather low 121 $ms^{-1} \cdot M^{-1}$ was obtained. Our particles are also bigger than Lu's (2) (60 nm average diameter, vs. 18 nm). This larger particle diameter adds a factor of 37 to the magnetic moment per particle, or 3 orders of magnitude to the relaxivity. These 2 effects (choice of material, particle diameter) add up to 5 orders of magnitude, which explain the difference between our results and Lu's results (2) on iron oxide. In figure 9 of Lu's paper, we can see that they require 10^{-4} M concentrations to observe an effect in the T_2-weighted contrast in phantoms. Our particles can be readily seen at 2.5×10^{-12} M in MRI images. This is a >7 orders of magnitude difference; this number includes the exponential effects of T_2-weighted contrast mentioned above. Cho et al. (3) report better results on Fe/Au nanoparticles, as would be expected for iron based on its high saturation magnetization, but they only report detectability thresholds of 300 pM in phantoms. (One could argue that the 300 pM cannot be seen in their figure 4, and the number is probably more like 600 pM. Also note that they report metal concentrations. The numbers we quote are converted to particle concentrations for comparison.) This number falls short of our cobalt nanoparticles detectability threshold. Their reported T_2 relaxivity, when converting the number 28.15 $mM^{-1} \cdot s^{-1}$ from their Table 1 to per-particle relaxivity (using 1 mM = 6 nM for iron particles of 18-nm diameter), we get $\approx 4 \times 10^6$ $mM^{-1} \cdot s^{-1}$, slightly lower than ours. Because fcc-Fe has a higher saturation magnetization, there is potential for even higher particle relaxivity

than cobalt by further increasing the particle diameter, but this is not demonstrated in their paper.

In Vivo Toxicity and Stability. Au nanoparticles are widely used in EM studies for live cells and no observable toxicity has been detected up to nM concentrations. Of all of the metal coatings examined so far, Au coatings have shown the lowest levels of toxicity. In animal studies, Au nanoparticles such as nanoshells have shown good dose tolerance. See refs. 4, 5, and 6 for relevant studies that establish the in vivo nontoxicity of Au particles. In dose-dependent studies, we have demonstrated (see Fig. S3) that up to micromolar concentration, Au nanoparticles induce no elevated apoptosis in cells.

Extension to Other Modalities. As shown in Fig. S4, there are situations where complementary information is crucial, as it is easy to find situations where single modality imaging will be insufficient. We believe that the combined PAT/MRI is extremely powerful for diagnostic imaging. MRI provides volume information whereas PAT provides edge detection. Our particles could certainly be used with position emission tomography (PET), using Au-coated radioactive cobalt, e.g., ^{60}Co, and CT; although both of these modalities are beyond the scope of this article. PAT, although in relative infancy compared to PET and CT, has the exciting possibility of providing edge-detection contrast, which is a definite advantage over MRI, and other imaging modalities.

PAT Imaging of Rat Tail Joints. CD hairless rats ($\approx$300 g; Charles River Laboratory) were included in this study. Whole tails were harvested from the rat bodies shortly after the rats were killed. An electrocautery device (SurgiStat; Valleylab) was then used to clot blood and seal vessels. Each rat tail was placed in the PAT system along the Z-axis as shown in Fig. S1. The first proximal segment of the rat tail was fixed on a rotational stage that, driven by a stepper motor, could rotate the tail around its axis. The imaged joint was about 2.5 cm from the rat trunk, where the diameter of the tail joint was 8–9 mm. First, a PAT image of a rat tail joint was taken before the administration of the contrast agent. After that, 0.05 mL of agent with a concentration of 100 pM was injected intraarticulary along the direction indicated by the arrows in Fig. S4B. Then another PAT image of the same joint was taken. The total numbers of nanowonton particles introduced into the regional joint tissue were on the order of 10^9 (i.e., femtomole). All of the experimental parameters for the images taken before and after the administration were kept the same, except that the sample might be moved slightly during the administration of contrast agent.

Cross-sectional imaging of the rat tail joint with and without injection of the nanowonton contrast agent (0.05 ml, 100 pM) are compared in Fig. S4 A and B. Following the administration of contrast agent, which perfused the front part of the joint space, hyperintensities are readily observed in the periosteum (Fig. S4B). With a comparatively limited detection bandwidth, the current PAT system is more sensitive to the edges of an absorbing object (arrow in Fig. S4B). Although the sensitivity of this PAT system to nanowonton contrast agent can be improved further by employing a laser source with better energy stability and a more sensitive transducer(s), this level of detection sensitivity is similar to or even higher than pure optical imaging for metallic particles (to). The general tendency of PAT to perform edge detection is evident when high frequency ultra-

sound detection is used. PAT with deeper penetration depth can be achieved by using laser light in the near infrared region, capitalizing on the ability to tune the absorption profile of the nanoparticles or the thin film coatings (Fig. S2). An anatomical section of the same tail joint is presented in Fig. S4C.

1. Hutten A, et al. (2004) New magnetic nanoparticles for biotechnology. *J Biotechnol* 112:47–63.
2. Lu J, et al. (2006) Solid-state synthesis of monocrystalline iron oxide nanoparticle based ferrofluid suitable for magnetic resonance imaging contrast application. *Nanotechnology* 17:5812–5820.
3. Cho SJ, Jarrett BR, Louie AY, Kauzlarich SM (2006) Gold-coated iron nanoparticles: a novel magnetic resonance agent for T_1 and T_2 weighted imaging. *Nanotechnology* 17:640–644.
4. Liao H, Nehl CL, Hafner JH (2006) Biomedical applications of plasmon resonant metal nanoparticles. *Nanomedicine* 1:201–208.
5. Cai Q, et al. (2007) Colloidal gold nanoparticles as a blood-pool contrast agent for X-ray computed tomography in mice. *Invest Radiol* 42:797–806.
6. Kim D, Park S, Lee JH, Jeong W, Jon S (2007) Antibiofouling polymer-coated gold nanoparticles as a contrast agent for in vivo X-ray computed tomography imaging. *J Am Chem Soc* 129:7661–7665.
7. Liu GL, et al. (2006) A nanoplasmonic molecular ruler for measuring nuclease activity and DNA footprinting. *Nat Nanotechnol* 1:47–52.
8. Loo C, et al. (2004) Nanoshell-enabled photonics-based imaging and therapy of cancer. *Technol Cancer Res T* 3:33–40.
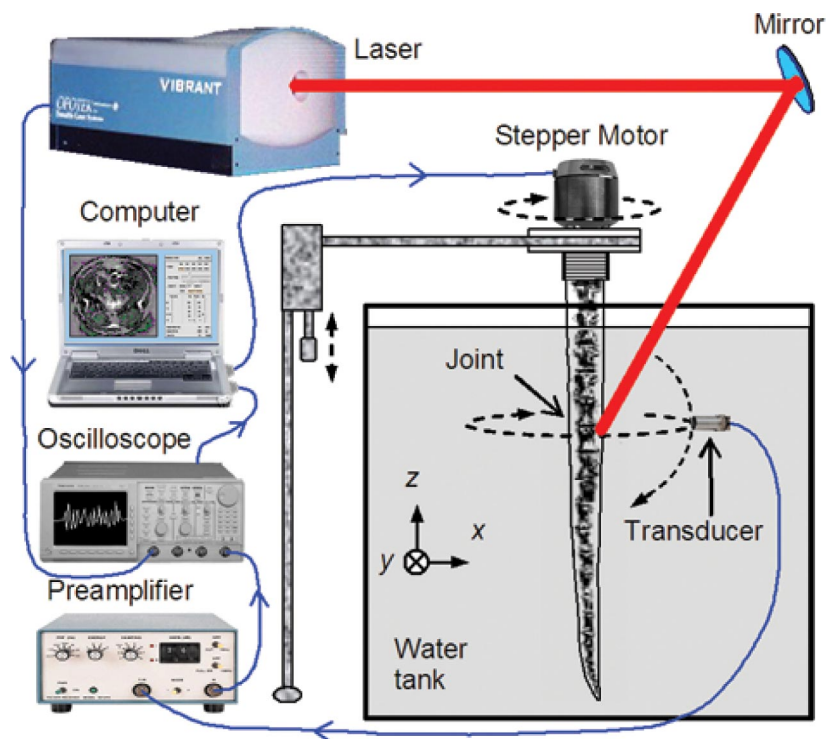
Fig. S1. Schematic of the PAT system.

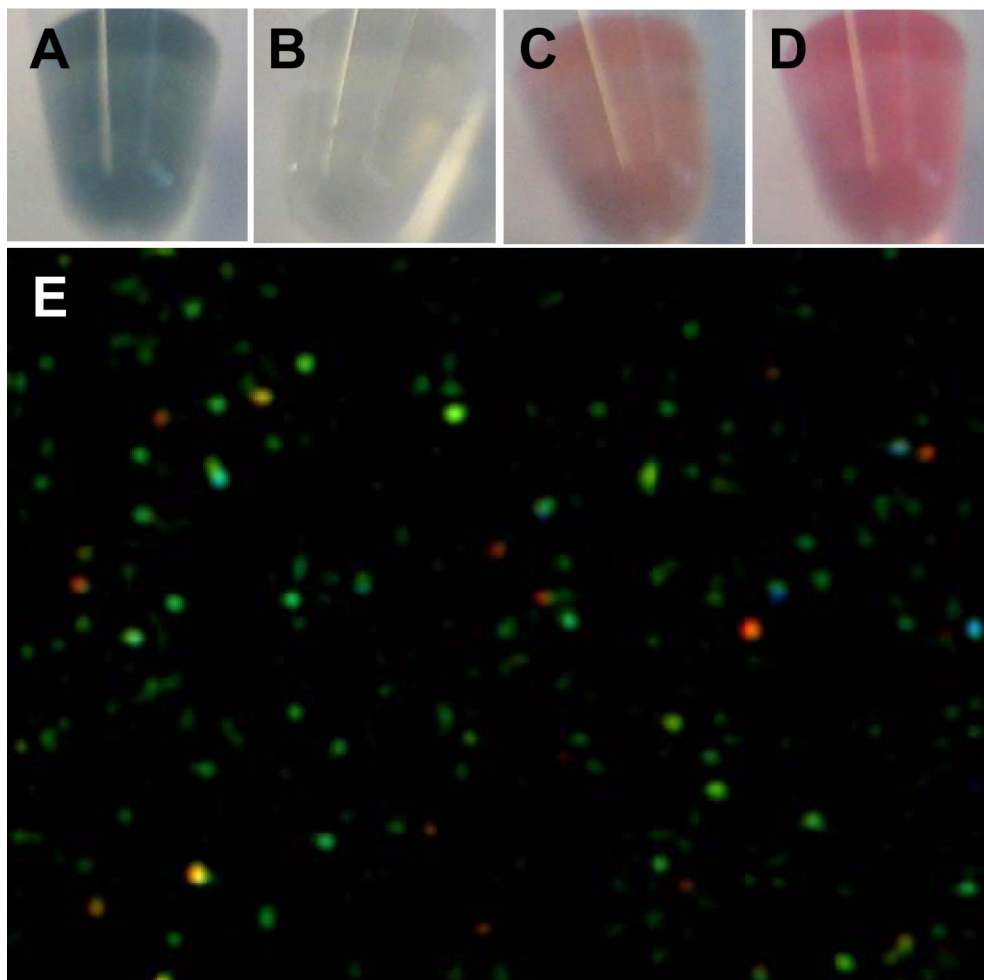**Fig. S2.** Schematic of Chinese wonton.

Fig. S3. Tunability of scattering wavelength of nanowonton by changing the size of the nanowonton. (*A*) The nanowonton with exterior diameter of 60 nm used in the study. (*B*) 80 nm diameter nanowonton. (*C*) 40 nm nanowonton. (*D*) A 10 nm nanowonton. (*E*) Scattering light microscopy image of the 60 nm diameter nanowonton with 700 nm peak scattering wavelength used in the study.
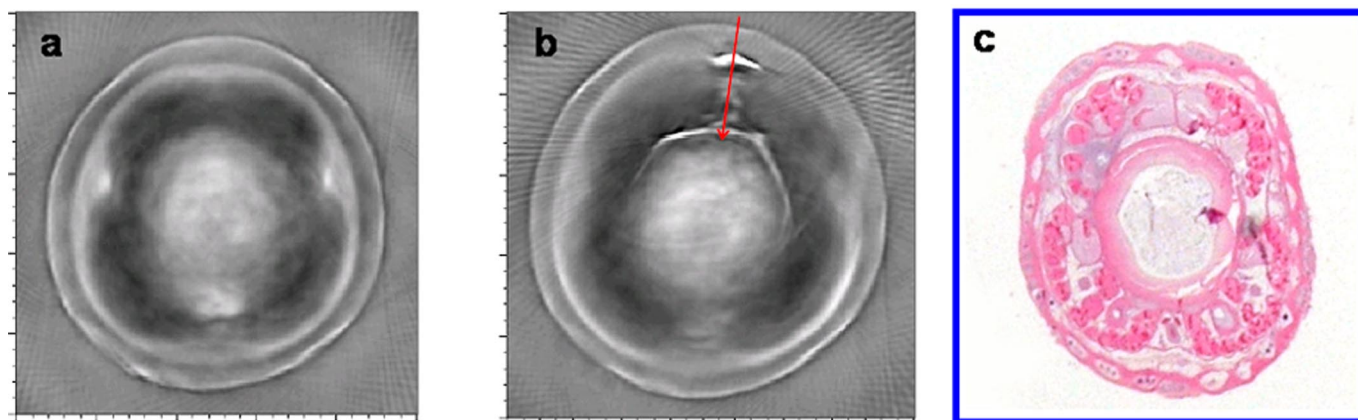
Fig. S4. Photoacoustic imaging of rat tail joint taken (*a*) before and (*b*) after the administration of nanowonton contrast agent at 100 pM. For comparison purpose, we also have obtained the (*c*) histological photograph of a similar cross section showing the periosteum. In *a* and *b*, grayscale is in arbitrary units of relative optical absorption, and *xy* scales are 1 cm × 1 cm.

Fig. S5. Au nanoparticles ranging from 2 to 200 nm are used to treat a model cell system (Jurkat cells) at 1.2 mg/L final concentration. Less than 1.2% of total cells show apoptosis. Result shows no significant difference from untreated cells, which have an apoptosis rate of 1%. The results show absence of toxicity with Au nanoparticles in the same size range.